J. Fluid Mech. (2003), *vol.* 488, *pp.* 1–29.
DOI: 10.1017/S002211200300466X Printed in the United Kingdom

The structure of fine-scale scalar mixing in gas-phase planar turbulent jets

By LESTER K. SU[1] AND NOEL T. CLEMENS[2]

[1]Department of Mechanical Engineering, The Johns Hopkins University, Baltimore, MD 21218-2681, USA

[2]Flowfield Imaging Laboratory, Center for Aeromechanics Research, Department of Aerospace Engineering and Engineering Mechanics, University of Texas at Austin, Austin, TX 78712-1085, USA

(Received 30 May 2002 and in revised form 7 February 2003)

Fine-scale scalar mixing in gas-phase planar turbulent jets is studied using measurements of three-component scalar gradient and scalar energy dissipation rate fields. Simultaneous planar Rayleigh scattering and planar laser-induced fluorescence, applied in parallel planes, yield the three-dimensional scalar field measurements. The spatial resolution is sufficient to permit differentiation in all three spatial directions. The data span a range of outer-scale Reynolds numbers from 3290 to 8330. Direct measurement of the thicknesses of scalar dissipation structures (layers) shows that the thicknesses scale with outer-scale Reynolds number as $Re_\delta^{-3/4}$, consistent with Kolmogorov/Batchelor scaling. Average layer thicknesses are described by the relation $\lambda_D = 14.5\,\delta\, Re_\delta^{-3/4} Sc^{-1/2}$. There is no evidence here that Taylor scaling ($\lambda_D \propto \delta\, Re_\delta^{-1/2}$) plays a significant role in the scalar dissipation process. The present data resolve a range of length scales from the dissipation scales up to nearly the jet full width, and thus can be used in *a priori* testing of subgrid models for scalar mixing in large-eddy simulations (LES). Comparison of two models for subgrid scalar variance, a scale-similarity model and a gradient-based model, indicates that the scale-similarity model is more accurate at larger LES filter sizes.

1. Introduction

Turbulent scalar mixing has been a subject of continual interest in fluid mechanics and associated fields. The mixing of two fluid streams is fundamentally important to a broad spectrum of engineering applications. In combustion systems, for example, molecular mixing of fuel and oxidizer is a necessary precursor to chemical reaction. The scalar dissipation rate, $\chi \equiv D\nabla C \cdot \nabla C$, where $C(\boldsymbol{x}, t)$ is a conserved scalar and D is the scalar diffusivity, is a quantity of particular interest to the understanding and modelling of turbulent non-premixed combustion. Mathematically, it represents the loss term in the evolution equation for $\frac{1}{2}C^2$, the scalar 'energy':

$$\left(\frac{\partial}{\partial t} + \boldsymbol{u}\cdot\nabla - D\nabla^2\right)\tfrac{1}{2}C^2 = -D\nabla C\cdot\nabla C \equiv -\chi. \tag{1.1}$$

Physically, χ can be interpreted as a mixing rate, or equivalently as a rate at which scalar fluctuations are destroyed. More specifically for combustion applications, Peters (1983) identified χ^{-1} as a characteristic diffusion time scale, imposed by the mixing field. Then, local flame extinction could be explained by the scalar dissipation

rate exceeding a critical value, thus making the diffusion time smaller than the chemical time of the local flame structure. Accurate representation of flame quenching and stabilization poses notable difficulties for computations of non-premixed flames, because dissipation of this scalar energy can occur at the finest mixing length scales of the flow. This means that modelling is required for the scalar dissipation rate in, for example, large-eddy simulations (LES) of turbulent non-premixed combustion, where the filtered mixture fraction is used as a starting point to describe the combustion.

Scalar mixing has also been studied with the aim of increasing the understanding of the physics of turbulent flows at small scales. Much effort has been devoted to assessing the validity of the universal similarity hypotheses of Kolmogorov (1941*a*, *b*, 1962) as applied to scalar fields. The work of Obukhov (1949), Corrsin (1951), Batchelor (1959), Batchelor, Howells & Townsend (1959) and others established that, where the scalar diffusivity and the kinematic viscosity are of comparable magnitudes, turbulent scalar field statistics at the small scales can be viewed analogously to the statistics of the turbulent velocity field. (For small and large scalar diffusivity, $D \ll \nu$ and $D \gg \nu$, respectively, additional mixing regimes arise that require extensions to the basic hypotheses.) Measurements of turbulent scalar fields thus provide an alternative means for assessing fundamental theories for turbulent flows.

Studies of turbulent scalar mixing have benefited a great deal from developments in laser-based flow diagnostic techniques. Planar measurement techniques such as planar Rayleigh scattering and planar laser-induced fluorescence (PLIF) afford direct experimental access to structural information in turbulent flows. Using these techniques it is possible to investigate directly such aspects of turbulent mixing as the topology of scalar mixing structures, the instantaneous distribution of mixing length scales, or fractal properties of mixing fields. Recognizing that turbulence is inherently three-dimensional, the possibility of extending these planar techniques to three dimensions is an attractive one. Three-dimensional measurements would obviate isotropy assumptions and other models intended to represent the full three-dimensionality of turbulent mixing from two-dimensional measurements.

Previous efforts at three-dimensional scalar field imaging in gas-phase flows have used either simultaneous two-plane Rayleigh scattering (Yip & Long 1986), or multi-plane scattering or PLIF, in which a single laser sheet is scanned through a three-dimensional volume (Yip *et al.* 1987; Yip, Schmitt & Long 1988). The former measurements, however, showed somewhat weak signal levels, while the latter technique suffers from temporal resolution limitations introduced by the laser sheet scanning. In particular, successive planes are both spatially and temporally distinct, compromising the interpretation of the data as purely three-dimensional in space. The liquid-phase measurements of Prasad & Sreenivasan (1990), Dahm, Southerland & Buch (1990) and Southerland & Dahm (1994) also involved the scanning of a single laser sheet. In those experiments, the higher kinematic viscosity of water resulted in time scales much longer than those in gas-phase flows at similar Reynolds numbers, minimizing the effect of temporal skewing between planes. To date, these experiments in water flows have represented the only extensive experimental studies of three-dimensional turbulent scalar mixing. However, the Schmidt number ($Sc \equiv \nu/D$) of water is three orders of magnitude higher than the Schmidt numbers typical of gases. Interpretation of water flow scalar measurements in the context of the gas phase (for combustion applications, for example) is, therefore, somewhat ambiguous.

Su & Clemens (1999) introduced an approach to three-dimensional scalar field imaging in the gas phase in which Rayleigh scattering and PLIF, applied simultaneously in separate planes, yield the three-dimensional scalar measurements.

This technique avoids the temporal skewing of scanning-based measurements, while the high efficiency of the fluorescence yields superior signal quality to two-plane Rayleigh scattering, for similar laser energy input. Su & Clemens (1999) described the implementation of the measurement technique in detail, and presented some preliminary analysis of the three-dimensional imaging data.

In this paper, we present a more extensive investigation of fine-scale turbulent mixing in the gas phase, using the three-dimensional turbulent scalar mixing data of Su & Clemens (1999). The flow considered in this study is a co-flowing, planar turbulent jet. The spatial resolution of the measurements is specified to resolve the expected finest scalar mixing length scale, using the estimate of this scale reported by Buch & Dahm (1998). The flow field and diagnostic method are discussed in § 2. Section 3 presents statistical analyses of the scalar power spectra and dissipation rate fields.

The primary goals of this study are to determine the magnitude of the dissipation, or inner, length scale of turbulent mixing and also the dependence of that scale on the flow outer-scale Reynolds number. In particular, we seek to confirm the $Re_\delta^{-3/4}$ scaling (Kolmogorov/Batchelor scaling) of the scalar dissipation length scale through direct measurement of three-dimensional dissipation field structures. Dowling (1991) used time-resolved single-point scalar concentration measurements to estimate the scalar dissipation rate, χ, and concluded that the smallest length scales indeed have a $Re_\delta^{-3/4}$ dependence. However, the estimation of χ from those data required both Taylor's hypothesis and the assumption of local isotropy, and the $Re_\delta^{-3/4}$ dependence was only inferred through a comparison with $Re_\delta^{-1/2}$ (Taylor) scaling; specifically, the dependence of the dissipation scale on Re_δ was not measured explicitly. A discussion of the definition of the dissipation length scale is given in § 1.1, and § 4 discusses the results for the magnitude and Reynolds number scaling of the dissipation scale obtained from the present measurements.

While advances in imaging technology have made possible direct access to large-scale turbulent structures, it is, conversely, partly through a recognition of the limits of computing technology that the field of turbulent flow simulation has arrived at structure-based methods, such as LES. At the intersection of these trends, experimental information of immediate use to LES is available. The present measurements, for example, encompass a range of scales from the dissipation scales up to nearly the full flow width, and thus offer great potential for *a priori* testing of LES subgrid models for scalar mixing. Section 5 presents sample results from *a priori* testing of two well-known subgrid models for the scalar variance, a gradient-based model and a scale similarity model. Finally, § 6 summarizes the major conclusions of this study.

1.1. *Dissipation length scale definitions*

Discussions of the dissipation length scales in turbulence are subject to some confusion because a variety of definitions are commonly used. Here we will outline the relationships among the various definitions. Kolmogorov's universal equilibrium hypothesis, that the small-scale properties of turbulence should be determined only by the rate of kinetic energy dissipation and the kinematic viscosity of the fluid (Kolmogorov 1941*b*), yields the Kolmogorov length scale

$$\eta \equiv (\nu^3/\epsilon)^{1/4}. \tag{1.2}$$

The Kolmogorov scale is often cited as the dissipation (or more strongly, smallest) length scale in turbulent flows. However, *a priori* it can at most be assumed that η is *proportional* to the dissipation length scale. In this paper, we will denote the

true turbulence dissipation length scale as λ_ν, which relates to the Kolmogorov scale through the proportionality constant Λ_K, as

$$\lambda_\nu = \Lambda_K \eta = \Lambda_K(\nu^3/\epsilon)^{1/4}. \tag{1.3}$$

Subsequent to the early work of Kolmogorov, Batchelor (1952) applied similar arguments to the problem of scalar mixing, and showed that the ratio of the dissipation scales in the velocity and scalar gradient fields depends on the square root of the Schmidt number, $Sc \equiv \nu/D$, where D is the molecular diffusivity. Analogously to the Kolmogorov scale, the Batchelor scale η_B is thus defined as $\eta_B \equiv \eta\, Sc^{-1/2}$, and we denote the scalar dissipation length scale as λ_D, where

$$\lambda_D = \Lambda_B \eta_B = \Lambda_B(\nu^3/\epsilon)^{1/4} Sc^{-1/2} \tag{1.4}$$

with proportionality constant Λ_B.

The dissipation length scales can be expressed in terms of outer-scale flow variables by using the relation $\epsilon \propto U^3/\delta$ (Taylor 1935). Then η scales as $\eta \propto \delta\, Re_\delta^{-3/4}$, where $Re_\delta \equiv U\delta/\nu$ is the outer-scale Reynolds number, and (1.3) and (1.4) become, respectively,

$$\lambda_\nu = \Lambda_\nu \delta\, Re_\delta^{-3/4}, \tag{1.5}$$

$$\lambda_D = \Lambda_D\, \delta\, Re_\delta^{-3/4} Sc^{-1/2}. \tag{1.6}$$

The proportionality constants Λ_ν and Λ_D will in general be different from the constants Λ_K and Λ_B in (1.3) and (1.4).

Quantifying the turbulence length scales can also proceed by noting that the thicknesses of structural features in the velocity or scalar gradient fields will be determined by the competing effects of compressive normal strain, which acts to make these structures thinner, and diffusion, which tends to thicken them. On the dissipative scales, the fluctuating normal strain rate is given by $s_{11} \propto (U/\delta)\, Re_\delta^{1/2}$ (e.g. Tennekes & Lumley 1972). If λ_ν is determined solely by s_{11} and the viscosity, ν, and if λ_D is determined by s_{11} and D, then we can derive (1.5) and (1.6) from dimensional considerations. Additionally, to a first approximation, the strain–diffusion mechanism should differ between the velocity and scalar gradient fields mainly in the diffusivities, which is accounted for by the Schmidt number. The proportionality constants in (1.5) and (1.6) should therefore be equal, or $\Lambda \equiv \Lambda_\nu = \Lambda_D$, giving

$$\lambda_\nu = \Lambda\, \delta\, Re_\delta^{-3/4}, \tag{1.7}$$

$$\lambda_D = \Lambda\, \delta\, Re_\delta^{-3/4} Sc^{-1/2}. \tag{1.8}$$

In the present work, we will measure the Re_δ dependence of the thicknesses, λ_D, of scalar dissipation structures directly, aiming to verify the $Re_\delta^{-3/4}$ scaling, and we will also estimate the proper value of the proportionality constant, Λ.

Based on estimates of the scalar dissipation rate from time-resolved single-point scalar concentration measurements, Dowling (1991) proposed an interesting adjunct to the interpretation of the dissipation length scale. While confirming that the smallest length scale that contributes to the scalar dissipation is λ_D, and that the bulk of the dissipation occurs at this scale, Dowling suggested that the highest dissipation rates occur at the larger Taylor scale, with a $Re_\delta^{-1/2}$ dependence. The Taylor scale can be interpreted physically as the length scale arising from a balance between the local outer-scale strain and diffusion; given the local outer-scale strain rate, $s \propto U/\delta$, the length scale dependent only on this strain rate and the viscosity is $\lambda \propto (\nu\delta/U)^{1/2} = \delta\, Re_\delta^{-1/2}$. Dowling thus concluded that the highest scalar dissipation rates occurred

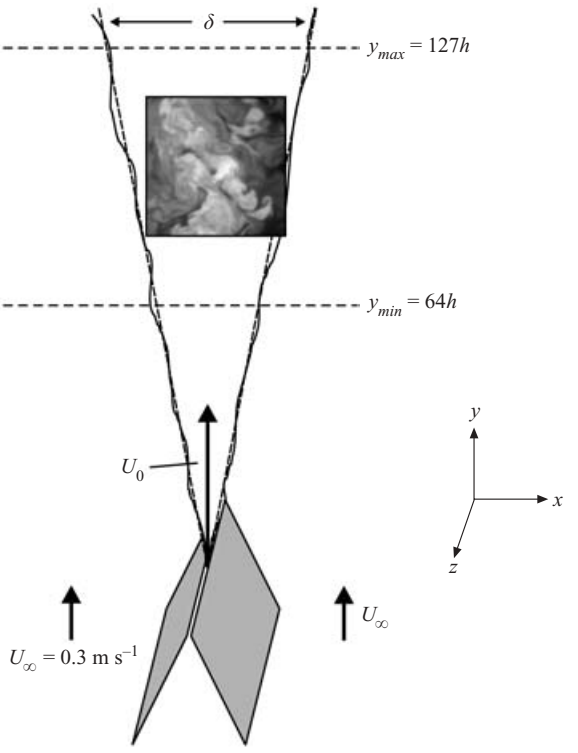

FIGURE 1. Sketch of the co-flowing planar turbulent jet, with a sample data plane from the set labelled f2 in table 1. Also indicated are the full width at 5% of maximum of the mean velocity profile, and the upstream and downstream limits of the measurement area for the full set of data.

in regions experiencing the strain rate of the outer, or energy-containing, flow scales. This hypothesis will also be explored in the present study.

2. Experimental conditions

This section describes the flow field in which the present measurements were performed, provides a brief description of the optical and diagnostic arrangement, and discusses spatial resolution and other issues related to the measurement of spatial gradients. Full experimental details can be found in Su & Clemens (1999).

2.1. *Flow field*

The flow field investigated here is a co-flowing planar turbulent jet. A schematic of this flow system is given in figure 1. The jet fluid consists of propane (C_3H_8), seeded with acetone (C_3H_6O) for diagnostic purposes (§ 2.2), while the co-flow consists of air. Acetone is seeded into the jet at approximately 5% by volume, so the jet fluid density, ρ_0, is roughly 1.54 times the density of the co-flowing air, ρ_∞. The jet nozzle has width $h = 1$ mm and spans 150 mm. A total of 37 data sets were acquired, each consisting of between 15 and 30 image pairs, for a total of 906 image pairs. Measurements were performed at positions ranging from $64h$ to $127h$ downstream of the nozzle exit. The imaging windows extend up to $21h$ off of the jet centreline in the cross-span direction. Table 1 lists the experimental conditions for each of the data sets. For all of the data sets, the co-flow velocity is $U_\infty = 0.3\,\mathrm{m\,s^{-1}}$.

Set (vols.)	U_0 (m s^{-1})	θ (h)	x (h)	y (h)	y_{max}/l_M	Re_δ	λ_D (μm)
a1 (30)	6.4	700	(−15, 19)	(65, 99)	0.26	[3770, 4630]	[510, 660]
b1 (30)	7.0	840	”	”	0.23	[4120, 5060]	[470, 610]
c1 (30)	7.1	860	”	”	0.22	[4180, 5140]	[470, 610]
d1 (30)	6.9	810	”	”	0.23	[4060, 4990]	[480, 620]
e1 (30)	6.0	620	”	”	0.28	[3530, 4340]	[530, 690]
f1 (29)	7.8	1040	”	”	0.20	[4590, 5640]	[440, 570]
g1 (18)	7.7	1010	”	”	0.20	[4530, 5570]	[440, 570]
h1 (30)	6.9	810	”	”	0.23	[4060, 4990]	[480, 620]
i1 (30)	5.6	540	(−13, 21)	”	0.30	[3290, 4050]	[560, 720]
j1 (30)	5.6	540	”	”	0.30	[3290, 4050]	[560, 720]
n1 (30)	7.5	960	(−15, 19)	(64, 98)	0.20	[4380, 5400]	[450, 580]
o1 (30)	8.2	1150	”	”	0.18	[4790, 5900]	[420, 540]
p1 (29)	8.4	1210	”	”	0.18	[4900, 6050]	[410, 530]
q1 (10)	9.4	1510	”	”	0.15	[5490, 6770]	[380, 490]
q1a (20)	10.0	1710	”	”	0.14	[5840, 7200]	[360, 470]
r1 (10)	9.5	1540	”	”	0.15	[5550, 6840]	[370, 480]
r1a (20)	9.2	1450	”	”	0.16	[5370, 6620]	[380, 500]
s1 (29)	9.6	1580	”	”	0.15	[5600, 6910]	[370, 480]
t1 (30)	8.2	1150	(−14, 20)	(70, 104)	0.19	[5010, 6080]	[440, 560]
u1 (30)	8.3	1180	”	”	0.19	[5070, 6160]	[440, 560]
v1 (30)	8.3	1180	”	”	0.19	[5070, 6160]	[440, 560]
w1 (30)	10.0	1710	(−16, 18)	”	0.15	[6110, 7420]	[380, 480]
x1 (30)	10.4	1850	”	”	0.14	[6350, 7710]	[370, 470]
y1 (30)	10.4	1850	”	”	0.14	[6350, 7710]	[370, 470]
z1 (30)	8.3	1180	(−14, 20)	(81, 115)	0.21	[5450, 6480]	[480, 590]
a2 (30)	8.5	1240	”	”	0.20	[5580, 6630]	[470, 580]
b2 (21)	8.5	1240	”	”	0.20	[5580, 6630]	[470, 580]
c2 (15)	10.6	1920	(−15, 19)	”	0.15	[6960, 8270]	[400, 490]
d2 (15)	10.1	1750	”	”	0.16	[6630, 7880]	[410, 510]
e2 (15)	9.9	1680	”	”	0.17	[6500, 7720]	[420, 520]
f2 (15)	10.0	1710	”	”	0.16	[6570, 7800]	[420, 520]
g2 (15)	9.0	1390	”	”	0.19	[5910, 7020]	[450, 560]
h2 (15)	8.3	1180	”	”	0.21	[5450, 6480]	[480, 590]
i2 (15)	9.2	1450	(−14, 20)	(93, 127)	0.20	[6470, 7540]	[480, 580]
j2 (15)	9.2	1450	”	”	0.20	[6470, 7540]	[480, 580]
k2 (15)	9.4	1510	”	”	0.20	[6620, 7710]	[470, 570]
l2 (15)	10.2	1780	”	(92, 126)	0.17	[7140, 8330]	[440, 540]
m2 (15)	9.3	1480	”	”	0.20	[6410, 7600]	[480, 580]
n2 (15)	9.2	1450	”	”	0.20	[6440, 7510]	[480, 580]

TABLE 1. Experimental conditions for the planar jet measurements. The jet exit excess velocity is U_0. θ is the momentum thickness defined in (2.1), in terms of the jet slot width, h. The x-range values are the cross-span limits of the imaging windows in terms of h, while the y values are the near- and far-downstream limits of the windows. y_{max}/l_M is the maximum downstream distance normalized by the length scale l_M, defined in (2.5), describing the relative importance of the momentum and buoyancy fluxes. The Re_δ values are the outer-scale Reynolds numbers at the near- and far-downstream limits, and the λ_D are the corresponding limiting values of the estimated dissipation length scale using $\Lambda_D = 11.2$ in (1.8).

The proper scaling regime for the co-flowing planar turbulent jet is determined through consideration of the momentum thickness, θ, defined in terms of the initial jet excess momentum flux (per unit nozzle span), J_0, as

$$J_0 = \rho_0 U_0^2 h = \rho_\infty U_\infty^2 \theta. \tag{2.1}$$

The resulting θ values for each data set are also given in table 1. Over the full set of data, the maximum value of y/θ in the imaging region is 0.183, at the furthest downstream measurement position in the sets i1 and j1. From Everitt & Robins (1978), this is well within the range for which pure jet scaling pertains, so jet scaling can be applied for all of the present data. The scalings for centreline velocity decay and flow width used here follow Bradbury (1965) and Everitt & Robins (1978):

$$U_c = 2.4 \left(\frac{\rho_0}{\rho_\infty}\right)^{1/2} U_0 \left(\frac{y}{h}\right)^{-1/2}, \tag{2.2}$$

$$\delta = \delta_{0.05} = 0.39\, y, \tag{2.3}$$

where U_c is the centreline jet excess velocity, and $\delta = \delta_{0.05}$ is the full width of the jet velocity profile at 5% of maximum. For the planar jet, then, the jet-exit Reynolds number is not adequate to describe local conditions, because the outer-scale Reynolds number $Re_\delta \equiv U\delta/\nu$ evolves in the downstream direction, with a $y^{1/2}$ dependence. (This contrasts with round jets, for which Re_δ is constant.) The minimum and maximum values of Re_δ for the individual data sets, defined using U_c from (2.2), δ from (2.3), and the kinematic viscosity of air at 1 atm and 300 K, $\nu = 0.155\,\mathrm{cm^2\,s^{-1}}$, are compiled in table 1. For the present data, Re_δ ranges from 3290 (in sets i1 and j1) to a maximum of 8330 (in set l2).

The discrepancy between the jet fluid density, ρ_0, and the ambient fluid density, ρ_∞, makes it necessary also to consider the effect of buoyancy in justifying the use of pure-jet scaling relations. We will assume that the results of Kotsovinos & List (1977) in positively buoyant planar turbulent jets can be applied to the current case of negative jet buoyancy. Let β_0 be the initial specific buoyancy flux per unit span, and m_0 the initial specific momentum flux, or

$$\beta_0 \equiv g\,\frac{|\rho_0 - \rho_\infty|}{\rho_\infty}\,U_0\,h, \quad m_0 \equiv J_0/\rho_0 = U_0^2 h, \tag{2.4}$$

where g is the gravitational acceleration. These can be combined to form a length scale, l_M, describing the relative importance of momentum and buoyancy fluxes, as

$$l_M \equiv \frac{m_0}{\beta_0^{2/3}}. \tag{2.5}$$

From Kotsovinos & List (1977), positively buoyant planar turbulent jets are momentum-driven, and follow jet-like scaling, for downstream positions $y/l_M \lesssim 0.4$. Table 1 lists y_{max}/l_M for each of the present data sets. The highest y_{max}/l_M is 0.30, for sets i1 and j1; the majority of the data have $y_{max}/l_M \leqslant 0.20$. The data are all thus in the momentum-driven regime, justifying the use of the jet scaling relations (2.2) and (2.3).

2.2. *Optical and diagnostic arrangement*

The current measurements are performed by simultaneous Rayleigh scattering and LIF in two parallel spatially distinct planes. This approach eliminates temporal skewing effects, while the high efficiency of LIF yields much higher signal levels for a given amount of laser energy than does two-plane Rayleigh scattering. In fact, for these experiments only a single frequency-doubled Nd:YAG laser is required. Propane was chosen as the jet fluid because its high index of refraction results in a Rayleigh scattering cross-section over 13 times that of air (Bartels *et al.* 1962; Eckbreth 1988). For the LIF, acetone is seeded into the jet fluid to approximately 5%

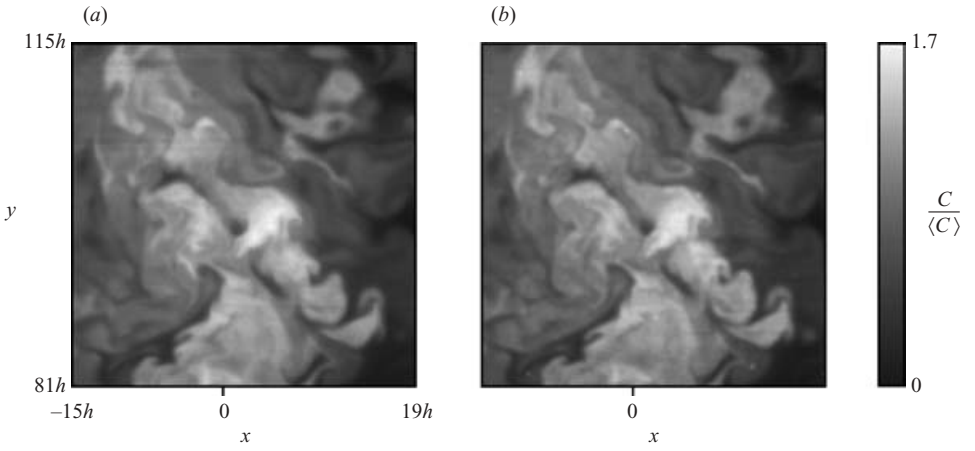

FIGURE 2. Scalar concentration fields measured by (*a*) PLIF and (*b*) Rayleigh scattering, from the set labeled f2 in table 1. The data planes are parallel and separated by 200 μm. The mean flow direction is upward in the images. The outer-scale Reynolds number, Re_δ, evolves from 6570 to 7800 in the measurement plane.

by volume. The 532 nm output of the laser is split so that 75% is used for the Rayleigh scattering, while the remainder is further frequency-doubled to 266 nm to excite the acetone LIF. The resulting laser sheet energies are typically 240 mJ/pulse at 532 nm and 30 mJ/pulse at 266 nm. To capture the signals, two slow-scan, thermoelectrically cooled CCD cameras, with 500×500 pixel resolution, are used. Optical filters ensure separation of the LIF signal (which peaks in the range 400–500 nm) from the Rayleigh scattering signal at 532 nm.

To obtain the scalar concentrations from the raw imaging signals, the acetone PLIF and Rayleigh scattering images are first filtered and binned by a factor of two to reduce noise, then mapped to the same imaging area and pixel resolution. Finally, standard background and laser sheet intensity profile corrections are performed, along with corrections for camera response non-uniformity and laser beam attenuation. For additional accuracy, the intensity profiles for the two laser sheets are captured for individual pulses rather than on an average basis. The resulting processed data planes span a 220×220 pixel grid, and cover a measurement window in the flow of 33.5×33.5 mm, giving a grid resolution of 152 μm. Figure 2 shows a sample scalar concentration field pair obtained by this simultaneous PLIF/Rayleigh scattering technique. The fields are taken from the set f2, for which the outer-scale Reynolds number ranges from 6570 to 7800. The location of the imaging region for this set relative to the mean jet evolution was shown in figure 1.

2.3. *Spatial resolution and gradient determination*

The objective of this study is to investigate the gradients of the scalar field, so high spatial resolution of the measurements is essential. The in-plane grid spacing was given above as $\Delta x = \Delta y = 152\,\mu$m. For all of these three-dimensional measurements, the two laser sheets are separated by $\Delta z = 200\,\mu$m. These resolution parameters should be compared with the estimated finest dissipation length scale, λ_D, defined in (1.8). Here we compute λ_D using $\Lambda_D = 11.2$ (Buch & Dahm 1998), and with the outer-scale parameters δ and Re_δ determined as described in § 2.1. The Schmidt number is found using the binary diffusivity of propane and air at 1 atm and 300 K,

$D = 0.114\,\mathrm{cm^2\,s^{-1}}$ (Reid, Prausnitz & Poling 1987) and the kinematic viscosity of air at the same conditions, $\nu = 0.155\,\mathrm{cm^2\,s^{-1}}$, giving $Sc = 1.36$. Because $\delta \propto y$ and $Re_\delta \propto y^{1/2}$, λ_D increases downstream of the jet exit, as $y^{5/8}$. Table 1 lists the minimum and maximum values of λ_D for the individual data sets. Over the full set of data, λ_D has a minimum value of 360 μm and a maximum value of 720 μm, with an average of $\langle \lambda_D \rangle = 510\,\mu\mathrm{m}$.

Normalizing the physical resolution parameters with λ_D, the in-plane grid resolution $\Delta x/\lambda_D\,(= \Delta y/\lambda_D)$ ranges from 0.21 to 0.42, averaging $\langle \Delta x/\lambda_D \rangle = 0.30$ over the full set of data, while the inter-plane spacing $\Delta z/\lambda_D$ ranges from 0.28 to 0.56, with $\langle \Delta z/\lambda_D \rangle = 0.40$. The Nyquist condition for critical resolution requires two data points for each characteristic length, i.e. $\Delta x_i/\lambda_D \leqslant 0.5$. Thus the data are fully resolved in the in-plane, x- and y-directions. In the out-of-plane, z-direction, the data are fully resolved except in limited portions of the imaging regions for the data sets q1, q1a, r1, r1a, s1, w1, x1 and y1, amounting to 179 of the 906 data volumes in the full set of present data. Any under-resolution is slight, as $\Delta z/\lambda_D$ exceeds the Nyquist value by no more than 12%.

It should be pointed out that the in-plane spatial resolution of the present measurements depends also on the resolution of the imaging cameras and camera optics, while the out-of-plane resolution depends also on the laser sheet thicknesses. Using a standard resolution target, it was found that the camera and optics used to collect the Rayleigh scattering signal had a true resolution equal to the grid spacing of 152 μm, while the true resolution of the PLIF camera and optics was only slightly worse, at 160 μm. The grid spacing $\Delta x = \Delta y = 152\,\mu\mathrm{m}$ is thus an accurate measure of the true in-plane resolution of the data. On the other hand, the minimum thickness of the 532 nm laser sheet was measured as 180 μm, while the minimum thickness of the 266 nm laser sheet was 200 μm, so the inter-plane spacing $\Delta z = 200\,\mu\mathrm{m}$ accurately represents the true out-of-plane resolution.

In measuring the three components, $\partial C/\partial x_i$, of the scalar gradient vector, the out-of-plane component (here, $\partial C/\partial z$) will be subject to the highest uncertainties, owing to the need to perform the difference calculation across distinct planes, which were obtained by different techniques and processed independently. The acetone PLIF and Rayleigh scattering signals are used as independent measures of the jet fluid concentration in the separate spatial planes, so accurate determination of $\partial C/\partial z$ requires that the propane and acetone in the jet fluid do not diffuse differentially into the ambient air, and that the data reduction is consistent for the two diagnostic techniques. Despite the difference in molecular weight between propane and acetone (44.10 vs. 58.08), their diffusivities in air are roughly equal, at $0.114\,\mathrm{cm^2\,s^{-1}}$ for propane, and $0.104\,\mathrm{cm^2\,s^{-1}}$ for acetone, at 300 K and 1 atm (Reid *et al.* 1987). To verify that the measurement of $\partial C/\partial z$ is not compromised by differential diffusion or data reduction errors, Su & Clemens (1999) applied the simultaneous PLIF/Rayleigh scattering technique in a single spatial plane, for which the scalar fields measured in the two imaging planes should be identical. Deviations from this were used to estimate the errors in the measurement of $\partial C/\partial z$ from the three-dimensional data. No systematic errors due either to differential diffusion or processing discrepancies were detected. Rather, errors in $\partial C/\partial z$ were found to be randomly distributed, with root-mean-square magnitudes on the order of 10% of the significant features in the $\partial C/\partial x$ and $\partial C/\partial y$ fields.

An interesting contrast arises between the present gas-phase measurements and prior measurements of the three-dimensional scalar gradient vector (Prasad & Sreenivasan 1990; Dahm *et al.* 1990; Southerland & Dahm 1994), which were

performed in water. From (1.8), at a given Reynolds number, the scale separation between the outer scale and the scalar dissipation scale, δ/λ_D, varies as $Sc^{1/2}$. For water, $Sc \approx 2000$, so the scale separation in water flows is nearly 40 times larger than that in the present measurements, where $Sc = 1.36$. As a result, resolving λ_D in water flows typically requires planar imaging windows with side dimensions much smaller than the local outer scale, δ. For measurements in water flows, then, resolving λ_D confines the range of length scales to the high-wavenumber dissipation range. The present measurements, however, resolve λ_D even though the width of the imaging windows is comparable to the outer scale, δ. The windows span 33.5 jet slot widths, h, while δ has a maximum value of $50h$ (from table 1 and (2.3)), so the imaging windows here span a minimum of 0.67δ. This wide span of the imaging windows, relative to the jet outer scale, is evident in figure 1. The present data thus permit analysis of scalar power spectra from the dissipation scales nearly to the integral scale, and also allow direct assessment of, for example, scale-similarity concepts for scalar and scalar dissipation rate fields, and subgrid models for scalar quantities in LES (§ 5).

2.3.1. *Determination of the Kolmogorov scale*

By applying previous results for the kinetic energy dissipation rate, ϵ, it is possible to estimate the Kolmogorov scale, η, for the present data using (1.2). Antonia, Satyaprakash & Hussain (1980) measured ϵ on the centrelines of planar turbulent jets, and established the following scaling in terms of the jet exit velocity, U_0, and the downstream coordinate, y:

$$\epsilon \approx 1.3 \frac{U_0^3}{h} \left(\frac{y}{h}\right)^{-5/2}, \tag{2.6}$$

where h is the jet nozzle width. To express this scaling in terms of local outer-scale variables, we use the relations (2.2) and (2.3) for the jet centreline velocity U_c and jet full width $\delta = \delta_{0.05}$ for the planar jet. Equation (2.6) then gives $\epsilon \approx 0.019\,(U_c^3/\delta)$, and applying this in (1.2), we obtain

$$\eta \approx 2.7\,\delta\, Re_\delta^{-3/4} \tag{2.7}$$

defining Re_δ in terms of U_c and δ. The estimated η for the planar jet is thus 0.28 times the value of λ_D estimated using $\Lambda = 11.2$, for the present $Sc = 1.36$. In § 2.3, the average λ_D for the full data set using $\Lambda = 11.2$ was given as 510 μm, so the average η is 143 μm. Normalized by η, the average in-plane grid spacing is $\langle \Delta x/\eta \rangle = 1.07$, and the average inter-plane spacing is $\langle \Delta z/\eta \rangle = 1.40$. The Batchelor scale, η_B, is given by $\eta_B \equiv \eta\, Sc^{-1/2}$, and with $Sc = 1.36$, η_B is 0.24 times λ_D, averaging 122 μm for the full data set.

3. Statistical results

3.1. *Spectral analysis*

Spectral theories for turbulent velocity fields have direct analogues in turbulent scalar fields, as explored in numerous studies (Obukhov 1949; Corrsin 1951; Batchelor 1959; Batchelor *et al.* 1959; Gibson & Schwartz 1963; Gibson 1968). For Schmidt numbers around unity ($D \approx \nu$), as in the present measurements, the power spectrum of scalar fluctuations (here, $E(k)$) should have a similar form to the spectrum of velocity fluctuations. In particular, for sufficiently high Reynolds numbers, one expects there to be an inertial range of wavenumbers k for which the scalar spectrum has a $k^{-5/3}$

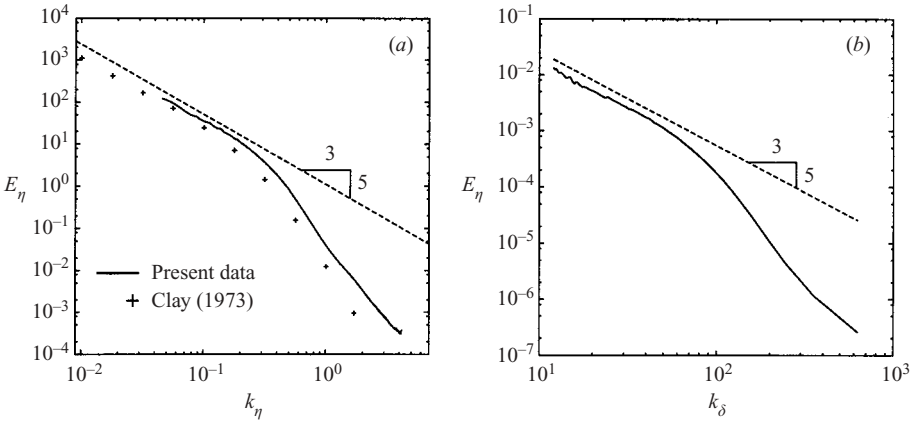

FIGURE 3. Averaged scalar power spectra for the present data, computed along data rows (i.e. fixed downstream position). (*a*) The Kolmogorov-normalized spectrum. The symbols are the data of Clay (1973) for temperature fluctuations in a heated turbulent air jet. (*b*) The spectrum normalized by outer-scale variables. Also shown on the plots is the expected inertial-range scaling $k^{-5/3}$.

dependence. For higher k, $E(k)$ falls off more rapidly as the 'energy' of the scalar fluctuations is dissipated.

In this section, one-dimensional scalar power spectra are computed for individual data rows, corresponding to fixed downstream positions in the jet. The data rows span a minimum of 0.67δ, and the measurement grid resolves the estimated λ_D, so the resulting spectra should encompass the dissipation range nearly up to the energy input range. We will be concerned here only with establishing the wavenumber dependence of the scalar spectrum. More quantitative analysis is compromised by certain characteristics of the data. Each data set contains at most 30 individual volumes, so the mean scalar fields for each set used to compute the scalar fluctuation fields are not fully converged. This limits the accuracy of the low-wavenumber portion of the spectrum in particular. This effect is countered by filtering the average scalar profile for each data row, using a top-hat filter with a radius of 20 grid points, prior to the determination of the scalar fluctuation values. Another property of the data that affects the quantitative interpretation of the scalar spectrum is that the highest resolved wavenumbers represent the expected characteristic dissipation length scales (§ 2.3). The use of finite-length data records (here, 220 points per record) inevitably corrupts numerically this range of wavenumbers. To mitigate this effect, a Welch window is applied to the data prior to the spectrum calculation.

Scalar power spectra for the full set of data, compiled by averaging the one-dimensional power spectra for fixed downstream positions y (individual data rows), are presented in figure 3. The spectra are computed for the normalized scalar fluctuations $C'(x, y) = (C(x, y) - \overline{C}(x, y))/\overline{C}_{max}(y)$, where the mean fields, $\overline{C}$, are determined for each data set, and $\overline{C}_{max}(y)$ is the local mean centreline value. With this normalization, the magnitude of the resulting spectrum for each row is effectively independent of downstream position. Because the relatively limited number of data volumes available compromises convergence and accuracy of $E(k)$ for low k, the averaged $E(k)$ shown do not include the three points at the low-k end of the spectrum for each data row.

In figure 3(*a*), the spectrum is presented in Kolmogorov-normalized form, with k made non-dimensional with η (as $k_\eta = k\,\eta$, with the local η found as described in

§ 2.3.1), and $E(k)$ normalized as $E_\eta = E/(\Sigma_\eta^2\,\eta)$, where Σ_η is the Kolmogorov scalar scale, defined (Gibson 1968) as

$$\Sigma_\eta = \left[\langle\chi\rangle(\nu/\epsilon)^{1/2}\right]^{1/2} = \frac{\langle\chi\rangle^{1/2}\eta}{\nu^{1/2}}. \tag{3.1}$$

Here $\langle\chi\rangle$ is the average dissipation value for each row, determined for each data set. In figure 3(b), the spectrum is shown normalized by outer-scale variables, with k normalized by the jet width, as $k_\delta = k\,\delta$, and E normalized as $E_\delta = E/\delta$. The moderate Reynolds number of the present data is manifested here in the limited k extent of the spectrum (roughly two decades). Despite the moderate Reynolds number, there is evidence in the plots of an inertial range with the expected $k^{-5/3}$ power-law dependence of $E(k)$. A least-squares fit to the Kolmogorov-normalized data (in the logarithmic axes) for $k_\eta < 0.2$ gives a slope $m = -1.623$. A least-squares fit to the δ-normalized data for $k_\delta < 50$ gives a slope $m = -1.627$.

The symbols in the Kolmogorov-normalized plot (figure 3a) are from Clay (1973), and represent the power spectrum of temperature fluctuations in a heated round air jet at a jet exit Reynolds number of 100 000. The scalar in that case being temperature, the relevant Schmidt number is the Prandtl number, where $Pr = 0.7$ in air. The spectrum of Clay is determined from time series data for temperature on the jet axis, and is converted to wavenumber units by Taylor's hypothesis. The spectrum for the present data is slightly displaced vertically from that of Clay in the presumed inertial range, which is probably due to details of the normalization of E_η. Specifically, in the determination of Σ_η (equation (3.1)), the present data use a spatial average for $\langle\chi\rangle$, while Clay employed an ensemble average at the measurement location to determine $\langle\chi\rangle$. The present $\langle\chi\rangle$ will thus be biased downward by low χ values at the edges of the jet, for example, which would be consistent with the slight overestimation of E_η in comparison with Clay's data. In the dissipation range, the data for the two Schmidt numbers are not expected to collapse in the Kolmogorov normalization; instead, the appropriate normalizing length scale is the Batchelor scale, $\eta_B \equiv \eta\,Sc^{-1/2}$ (Gibson 1968). In figure 3(a), then, the present spectrum should be displaced from that of Clay in the dissipation range by $\log_{10}(Sc/Pr)^{1/2} = \log_{10}(1.36/0.7)^{1/2} = 0.14$ decades in the logarithmic axes. The actual horizontal displacement of the two spectra at $E_\eta = 0.1$ is ≈ 0.16 decades, so the discrepancy between two spectra in the dissipation range is quite consistent with theory.

The existence of an inertial range in the spectra of figure 3 would suggest that, for wavenumbers above the dissipation range, the details of the energy input process in the scalar mixing have become unimportant for the Reynolds numbers considered. It is surprising that there should be any evidence for an inertial range at the present modest Reynolds numbers, which fall short of the value of $Re_\delta \approx 20\,000$ proposed as a fully developed turbulence criterion by Dimotakis (2000). However, that criterion is based on consideration of the so-called mixing transition (Konrad 1976; Roshko 1991; Catrakis & Dimotakis 1996), which assesses the mixing in terms of the spatial density of unmixed fluid in the flow, and does not make explicit reference to spectral properties. The present data suggest that the scalar spectra can show an inertial range at Reynolds numbers below the mixing transition. The evidence for an inertial range in the present data provides support for the generality, to higher Reynolds numbers, of the results for the structural properties of small-scale turbulent mixing presented in this paper.

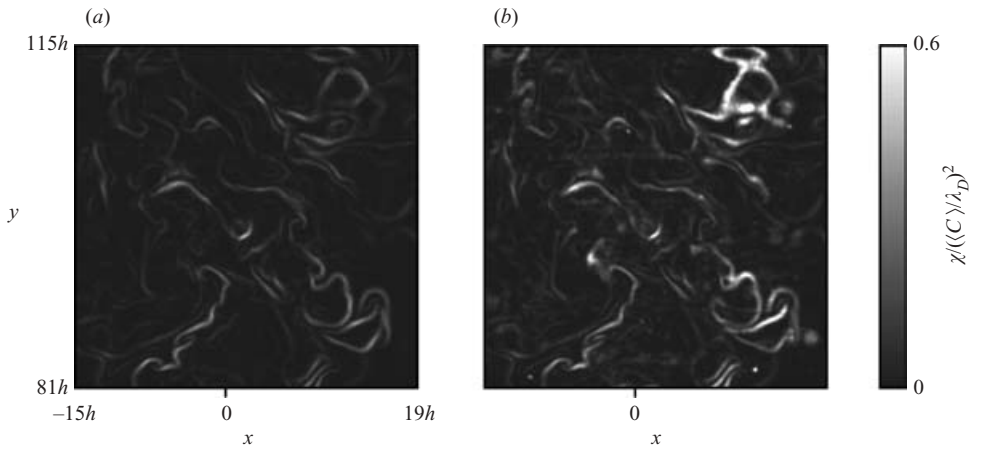

FIGURE 4. Scalar dissipation rate fields for the scalar concentration field of figure 2. (*a*) The two-component scalar dissipation rate field, χ_{2D}, determined from the in-plane scalar gradient components, $\partial C/\partial x$ and $\partial C/\partial y$, of the PLIF concentration field. (*b*) The three-component field, $\chi = \chi_{3D}$. The out-of-plane component, $\partial C/\partial z$, was determined by differencing between the PLIF and Rayleigh scattering fields.

3.2. *Dissipation rate field statistics*

Figure 4(*a*) shows the two-component scalar dissipation rate field, χ_{2D}, determined from the scalar field data volume of figure 2. The in-plane components, $\partial C/\partial x$ and $\partial C/\partial y$, of the scalar gradient vector, ∇C, were computed using central differences around each grid point in the PLIF data plane. Figure 4(*b*) shows the full three-component dissipation rate field, $\chi = \chi_{3D}$, for the same data volume. The out-of-plane component, $\partial C/\partial z$, of ∇C was computed by a two-point difference between the PLIF and Rayleigh scattering data planes. From figure 4 it is clear that structures in these planar measurements of χ are characteristically thin, with lengths well in excess of their thicknesses, corresponding to lamellar or layer-like structures in three dimensions. The tendency of the scalar dissipation rate field to be organized in layers has been noted previously in, for example, the experiments of Buch & Dahm (1996, 1998) and Southerland & Dahm (1994).

Statistics of the scalar dissipation rate field, particularly the form of its probability density function (PDF), are of interest for quantifying the intermittency of turbulent mixing. Here as well theories for scalar energy dissipation have been developed by analogy with kinetic energy dissipation. Obukhov (1962) and Kolmogorov (1962) hypothesized that kinetic energy dissipation followed a log–normal distribution. Subsequently, Gurvich & Yaglom (1967) extended this log–normal hypothesis to scalar energy dissipation. The form of the PDF of χ is fundamental to simulations of non-premixed turbulent reacting flows. In large-eddy simulations, dissipation generally occurs on the subgrid scales and is subject to modelling. The assumption of log–normality of the PDF of χ is commonly used in LES of combustion (e.g. Bushe & Steiner 1999).

Dahm & Buch (1989) presented results for the χ PDF based on the single-component scalar gradient measurements of Dowling & Dimotakis (1990) in gas-phase turbulent jets. The PDF of the three-component dissipation rate, χ, was determined from the single-component measurements χ_{1D} by assuming isotropy of the

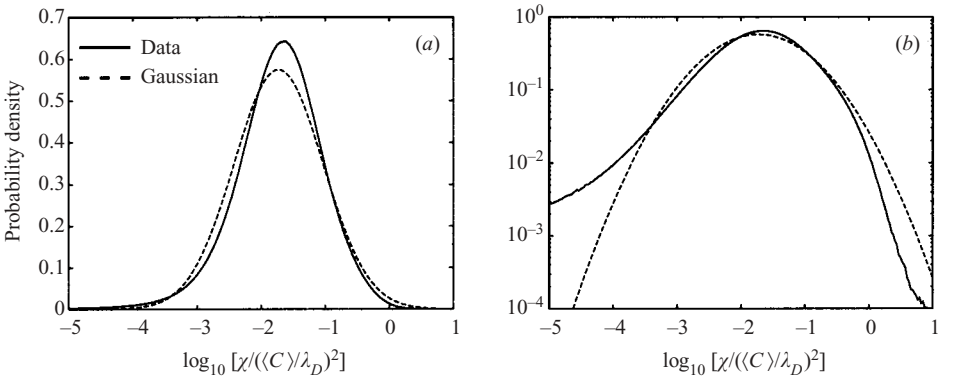

FIGURE 5. The PDF of the logarithm of the scalar dissipation rate, χ, with (*a*) linear and (*b*) logarithmic *y*-axis, compared with the Gaussian distribution having the same first two moments. The mean value of χ is indicated. The χ distribution shows a small negative skewness.

scalar gradient. Buch & Dahm (1996, 1998) applied a similar procedure to determine the χ PDF from measurements of the two-dimensional dissipation rate, χ_{2D}, in both gas- and liquid-phase jets. The χ PDFs for the gas-phase data, estimated from the measurements of both χ_{1D} and χ_{2D}, were found to be very nearly log–normal. For the liquid-phase data, Buch & Dahm (1996) found slight but noticeable departures from log–normality in the χ PDF. In particular, the data show a slight negative skewness (third moment). Subsequent to these experiments, Southerland & Dahm (1994) performed direct measurements of the three-component χ in a liquid-phase jet, and also found small departures from log–normality of the χ PDF, manifested in negative skewness.

Figure 5 shows the PDF of the logarithm of χ for the present three-dimensional measurements, with both linear and logarithmic *y*-axis. Scalar values are normalized by the mean scalar concentration, $\langle C\rangle$; the grid spacings Δx_i used in the finite differencing are normalized by the estimated dissipation scale, λ_D, found using (1.8) and with $\Lambda = 11.2$ as recommended by Buch & Dahm (1998). Also shown in the figure is a Gaussian distribution having the same first two moments. The χ distribution is evidently nearly log–normal, though, as with the liquid-phase data of Buch & Dahm (1996) and Southerland & Dahm (1994), departures from the Gaussian curve come in the form of small negative skewness. The negative skewness is more evident in figure 5(*b*).

If one assumes that the log–normal distribution is the true form of the turbulent χ PDF, possible explanations for the departure from log–normality in figure 5 include the presence of the jet outer boundary in some of the images (where the presence of unmixed ambient air increases the population of low χ values), the moderate Reynolds number of the data, and the effects of finite resolution and measurement noise. To illustrate the first of these points, observe (from table 1 and using (2.3)) that for the most-upstream data row in set n1, the jet width is $\delta = 25.4h$, so that row spans $-0.59 < x/\delta < 0.75$. Since δ is the jet full width, this means that the data row encompasses regions where the jet fluid concentration C, and χ, are expected generally to be near zero. To minimize this effect in the χ PDF, figure 6 shows the χ PDF conditioned on $|x/\delta| \leqslant 0.28$, compared with the full χ PDF from figure 5. The $|x/\delta| \leqslant 0.28$ limit is the largest symmetric interval covered by all of the data rows.

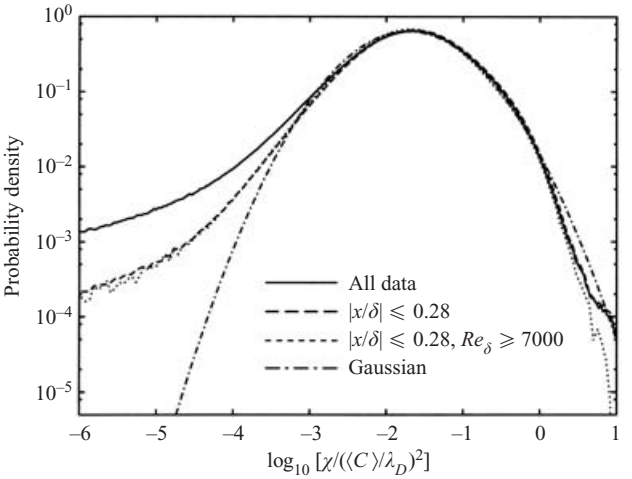

FIGURE 6. The PDF of the logarithm of χ from figure 5, along with the PDFs conditioned on cross-span position $|x/\delta| \leqslant 0.28$, and conditioned on both $|x/\delta| \leqslant 0.28$ and $Re_\delta \geqslant 7000$. The Gaussian distribution shown is the fit to the PDF conditioned on both $|x/\delta|$ and Re.

Conditioning the χ distribution clearly increases the agreement with the log–normal distribution.

The moderate Reynolds number of the data might also explain the departure from log–normality of the χ PDF, as the equilibrium hypotheses for high Reynolds numbers would be less valid. Additionally, at higher Reynolds number, the flow would be more likely to have begun (or undergone) the mixing transition, after which there would be a sharp reduction in the spatial density of unmixed fluid with χ near zero. Thus the moderate Reynolds number of the data might affect the χ PDF similarly to the inclusion of the jet outer boundary in the measurements. To assess the Reynolds number effect on the χ distribution, figure 6 also shows the χ PDF conditioned on both $|x/\delta| \leqslant 0.28$ and local $Re_\delta \geqslant 7000$. Compared with the conditioning on $|x/\delta| \leqslant 0.28$ alone, the additional Re_δ conditioning appears to reduce slightly the probability of low χ values. At the same time, the Re_δ-conditioned PDF drops off more steeply at high χ values, similarly to the log–normal distribution.

The pronounced skewness of the PDF remains, however, even conditioning on high Re_δ. It is possible that the observed preponderance of low χ values is due to well-mixed, rather than nearly-unmixed, fluid, and that the departure from log–normality is the true form of the χ PDF for high Re_δ. This may be Schmidt-number dependent. Indeed, in the present gas-phase scalar mixing images, unmixed fluid regions are far less evident than in the liquid-phase measurements of Buch & Dahm (1996) and Southerland & Dahm (1994). Dimotakis (2000) also noted that gas-phase flows show more homogeneous scalar fields than liquid-phase flows at similar Reynolds numbers.

Another possibility is that the skewness might be an experimental artifact, and arises from either measurement noise or inadequate spatial resolution. We would, *a priori*, expect that noise can be ruled out as a possible explanation, since noise would tend to cause an under-population of the low values in the χ PDF, counter to the negative skewness observed in figures 5 and 6. Figure 7(*a*) shows the distributions of χ computed both for the raw data, and for the data as contaminated by synthetically generated random noise. The noise followed a Gaussian distribution, with variance equal to 0.02 times the average scalar value, $\langle C\rangle$. It is clear from figure 7(*a*) that the

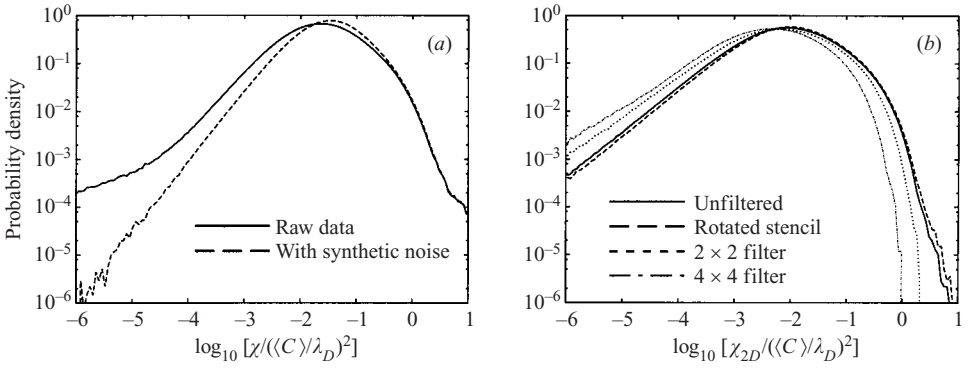

FIGURE 7. The effects of measurement noise and spatial resolution on the PDFs of the scalar dissipation rate, conditioned on $|x/\delta| \leqslant 0.28$. (*a*) PDFs of the logarithm of χ for the raw data, and for the data as contaminated with synthetic random noise. (*b*) PDFs of the logarithm of χ_{2D} for the raw data, for the raw data using the rotated differencing stencil, and for the data after 2×2 and 4×4 box filtering.

effect of noise is to introduce a positive skewness bias, confirming that measurement noise is not the cause of the observed negative skewness of the χ PDF.

However, inadequate resolution of scalar gradients by the imaging system could lead to over-representation of low χ values and under-representation of high χ values in the χ PDF. To see if resolution effects might explain the full quantitative discrepancy between the measured χ distributions and the log–normal curve, the distributions of the two-dimensional scalar dissipation rate, χ_{2D}, were computed for the data at different levels of deliberately reduced resolution. This resolution test used χ_{2D}, computed using the $\partial C/\partial x$ and $\partial C/\partial y$ components of the scalar gradient vector, rather than the full three-dimensional χ, because there are only two data planes in the z-direction and thus the resolution of the $\partial C/\partial z$ component cannot be artificially reduced. Recognizing that the grid-centred central difference operator implicitly filters the data to some degree, χ_{2D} was also computed using a differencing stencil rotated by 45°. That is, given a point (i, j) in the data plane, one component of χ_{2D} is found by differencing between the points (i, j) and $(i-1, j-1)$, and the other is found by differencing between the points $(i-1, j)$ and $(i, j-1)$. Computing χ_{2D} in this way also represents a central difference, in this case around the off-grid point $(i-1/2, j-1/2)$, though the effective grid spacing is smaller by a factor of $\sqrt{2}$ compared with grid-centred central differencing. Figure 7(*b*) shows the χ_{2D} PDFs for the original, 220×220 data planes, the 110×110 planes resulting after 2×2 box filtering of the data, and the 55×55 planes resulting from 4×4 box filtering, all found through grid-centred central differencing, and the χ_{2D} PDF for the raw data found using the rotated differencing stencil. All of the PDFs are conditioned on $|x/\delta| \leqslant 0.28$. While the data with artificially reduced resolution show higher skewness than the unfiltered data, the discrepancy is small. At the low-χ_{2D} end of the distribution in figure 7(*b*), each factor of two reduction in resolution raises the probability density by roughly a factor of two. Comparing the χ_{2D} distributions for the unfiltered data using the grid-centred and rotated differencing stencils, the filtering effect of the grid-centred central difference operator is slight, and is in fact smaller than the effect of the 2×2 box filter. (Grid-centred central differencing is used for the remainder of the present work, because the computed $\partial C/\partial x$ and $\partial C/\partial y$ components can then be associated with the same spatial points as the computed $\partial C/\partial z$; this condition does not hold for

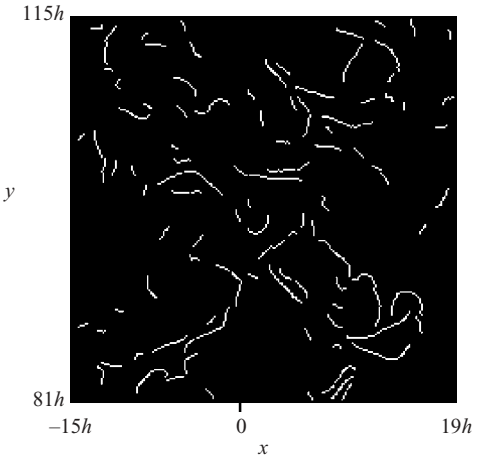

FIGURE 8. The dissipation layer centres determined from the χ field of figure 4(b).

the rotated differencing stencil.) From the results of figure 7(b), it appears unlikely that the departure from log–normality of the scalar dissipation rate distribution seen in figures 5 and 6 can be fully explained by deficient resolution. It instead appears that a slight negative skewness is a property of the scalar dissipation rate PDF.

4. Dissipation length scales

In a turbulent shear flow, the thickness of the dissipation layers will scale with the local outer-scale Reynolds number, Re_δ. The form of this Re_δ dependence was explored in § 1.1. In this section, we investigate the dependence by direct measurement of the thicknesses of the layers. We will also be able to determine the proper value of the proportionality constant in the scaling relation.

Figure 8 shows the dissipation layer centres for the three-component scalar dissipation rate field of figure 4(b). This layer centre field was compiled by first identifying peaks in the dissipation field. A given point was determined to be a 'peak' if the local dissipation rate both exceeded a given threshold and represented the local maximum value in both the positive and negative in-plane scalar gradient vector directions. A connectivity condition was then imposed on the peak field to remove noise effects. For figure 8, the threshold value was that which captures 75% of the total dissipation for the full data set (namely, non-dimensional $\chi = 0.058$). The connectivity condition required that the dissipation structures span a minimum length of twice the estimated value of λ_D, determined from (1.8) and using $\Lambda = 11.2$.

Determination of the layer centre fields represents the first step in the measurement of the layer thicknesses. We define the local layer thickness for a given point on a dissipation layer, λ_{loc}, as the full width of the layer, where this width is computed as the distance across the layer between those points where the dissipation rate is 20% of the maximum. For each of the points in the layer centre fields, a search is performed in the in-plane scalar gradient direction (both positive and negative) until the dissipation value drops below 20% of the maximum. The exact point at which the dissipation is 20% of the maximum value is approximated through linear interpolation between the last two points in the search. The resulting layer half-width values are then doubled to give a measure of the full width, λ_{loc}. For those layers where the dissipation rate fails to drop monotonically, indicating a possible intersection of

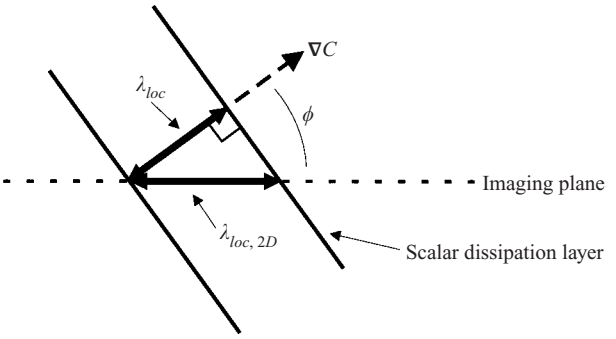

FIGURE 9. Measurement of the local layer thickness, λ_{loc}, for a planar scalar dissipation layer intersecting the imaging plane obliquely. Here $\lambda_{loc} = \lambda_{loc,2D}\cos\phi$, where $\lambda_{loc,2D}$ is the thickness measured in the imaging plane, and ϕ is the out-of-plane angle of the scalar gradient vector.

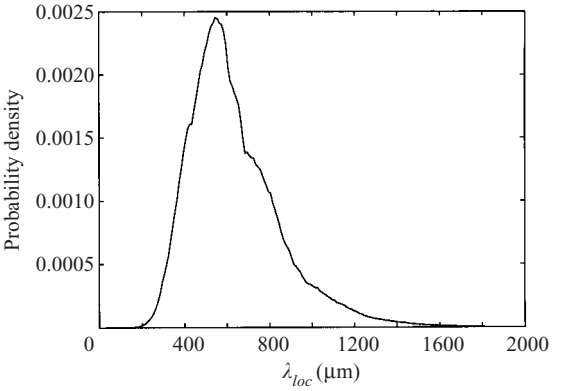

FIGURE 10. The probability distribution of the local scalar dissipation layer thickness, λ_{loc}, for the full set of present data.

layers, statistics are not compiled. Finally, because the dissipation rate images, and thus the thickness computations, are strictly two-dimensional, the resulting thicknesses are adjusted to account for three-dimensionality, by using the known orientation of the three-dimensional scalar gradient vector, ∇C. Figure 9 illustrates this correction for the idealized case of a planar dissipation layer, in which the scalar concentration varies only in the layer-normal direction. The true value of λ_{loc} is found from $\lambda_{loc,2D}$, the value determined using the two-dimensional algorithm, as

$$\lambda_{loc} = \lambda_{loc,2D}\cos\phi, \tag{4.1}$$

where ϕ is the out-of-plane angle of ∇C. This correction becomes less reliable as the dissipation layer becomes more closely aligned with the imaging plane, i.e. as ϕ increases. The effects of layer curvature, and of non-zero scalar gradients in the layer-parallel directions, may then become significant. For this reason, only dissipation maxima where $\phi \leqslant 60^\circ$ were considered.

Figure 10 shows the raw dissipation layer thicknesses for the full set of data. The threshold value of the dissipation rate, χ, and the connectivity condition used in the layer definition are the same as applied in figure 8. The peak of the thickness distribution in figure 10 lies at just under 600 μm, while the thinnest layers in the distribution are just under 200 μm thick, and the thickest layers just over 1600 μm

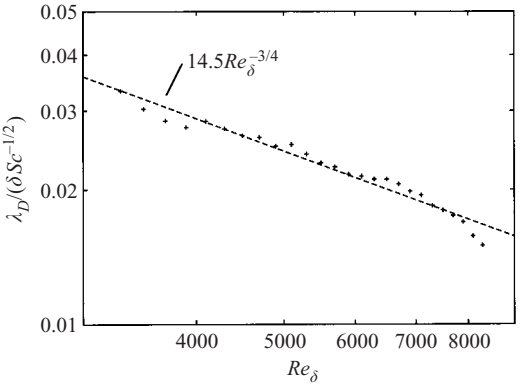

FIGURE 11. The average dissipation layer thickness conditioned on the local outer-scale Reynolds number. The dashed line is the curve $14.5Re_\delta^{-3/4}$.

thick. Recalling that the in-plane grid spacing of the data is $\Delta x = 152\,\mu\text{m}$, the peak of the thickness distribution lies at approximately $4\,\Delta x$; the thinnest layers, on the other hand, measure roughly $1.3\,\Delta x$, and the thickest layers measure roughly $10.5\,\Delta x$. Interestingly, the in-plane grid spacing, Δx, places a lower bound only on the two-dimensional layer thickness, $\lambda_{loc,2D}$, that can be resolved. Because $\lambda_{loc} \leqslant \lambda_{loc,2D}$ (equation (4.1)), figure 9 illustrates that, with the present three-dimensional measurements, the ability to resolve the true, three-dimensional layer thickness is in principle better than would be implied by the in-plane grid spacing alone. In the light of this, and since the thicknesses of smallest layers in the distribution of figure 10 exceed Δx, it appears that the measurement of λ_{loc} is not noticeably compromised by the in-plane measurement resolution.

As mentioned earlier, at issue in the computation of layer thicknesses are the proper Re_δ scaling of the characteristic scalar dissipation scale, λ_D, and the proper value of the coefficient in the scaling relation for λ_D. We will define λ_D here as the average of the local dissipation layer full widths, λ_{loc}. This definition of λ_D is consistent with that of Buch & Dahm (1998). To isolate the dependence of λ_D on Re_δ, the local outer-scale Reynolds number, we will assume that the δ and Sc dependence in (1.8) is correct, and consider the quantity $\lambda_D/(\delta\, Sc^{-1/2})$.

Figure 11 shows $\lambda_D/(\delta\, Sc^{-1/2})$ as a function of Re_δ, in log–log axes. Again, as with figures 8 and 10, the threshold value of χ is chosen to capture 75% of the total dissipation, and the layers are required to have a minimum length of twice the estimated λ_D. The curve is generated by first dividing the Reynolds number range 3200 to 8400 into 26 bins, then finding the average value of $\lambda_{loc}/(\delta\, Sc^{-1/2})$ in each bin. The least-squares linear fit to the data in these log–log axes has a power law dependence $Re_\delta^{-0.74}$. The dashed line in the plot is the curve $14.5Re_\delta^{-3/4}$, where the coefficient is found by a least-squares fit to an imposed $Re_\delta^{-3/4}$ dependence. From this plot it is evident that the average dissipation layer thicknesses follow the $Re_\delta^{-3/4}$ Batchelor/Kolmogorov scaling given in (1.8).

Dowling (1991) suggested (§ 1.1) that while the majority of the dissipation occurred at scales that followed Batchelor/Kolmogorov scaling, a substantial portion of the dissipation, in particular the highest local dissipation values, occurred at the larger Taylor scale, with a $Re_\delta^{-1/2}$ dependence. If true, thicker layers should be measured if the threshold value of the dissipation rate is increased. Table 2 shows the results from the determination of layer thicknesses for different threshold values of χ. The

χ_{min}	% tot. diss.	Λ
0.006	99	14.6
0.026	90	14.6
0.058	75	14.5
0.078	67	14.5
0.142	50	14.2
0.342	25	13.4

TABLE 2. Dependence of layer thicknesses on the threshold value of the scalar dissipation rate, χ. Only layers with peak χ exceeding χ_{min} are used in compiling the thickness statistics. The percentages of the total scalar dissipation captured with these χ_{min} are given in the second column in the table. The value of the coefficient Λ is found by a least-squares fit to the average thickness vs. Re_δ data (as shown in figure 11), where a dependence of $Re_\delta^{-3/4}$ is imposed.

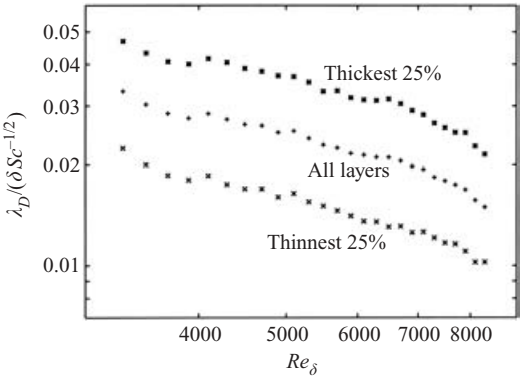

FIGURE 12. Dissipation layer thickness conditioned on the local Re_δ. Shown are the average thicknesses of the thickest 25% of layers, the thinnest 25% of layers, and all layers.

results are presented in terms of the value of the scaling coefficient Λ in (1.8). These Λ are determined (as in figure 11) by finding the least-squares fit of $Re_\delta^{-3/4}$ curves to the data for $\lambda_D/(\delta\, Sc^{-1/2})$ vs. Re_δ, where the λ_D are the average dissipation layer thicknesses. As seen in the table, higher threshold values of χ result in *thinner* layers (smaller Λ), arguing against a greater importance of the larger Taylor scale for higher dissipation rates.

The possible contribution of Taylor scaling to the dissipation can also be assessed by considering the Re_δ dependence of the extremes of the layer thickness distribution. Figure 12 shows the Re_δ dependence of the average thickness of the thickest and thinnest 25% of layers. These curves are compiled by determining the average value for the upper and lower 25% of the $\lambda_{loc}/(\delta\, Sc^{-1/2})$ distribution in each Re_δ bin. Also shown in the figure is the overall average shown in figure 11. There is essentially no evidence in these curves of any $Re_\delta^{-1/2}$ scaling of the thickest layers. The least-squares fit to the $\lambda_D/(\delta\, Sc^{-1/2})$ curve for the thickest 25% of layers has dependence $Re_\delta^{-0.73}$, while the fit to the curve for the thinnest 25% has dependence $Re_\delta^{-0.75}$. The trend of weaker Re_δ dependence (smaller magnitude of the exponent) for thicker layers is consistent with Dowling's hypothesis, but this difference of -0.73 and -0.75 in the exponent is within experimental tolerances, and gives no indication of $Re_\delta^{-1/2}$ scaling.

It should be pointed out that at moderate Reynolds numbers such as those of the present study, the Taylor scale might become of the same order as, or smaller than,

the $Re_\delta^{-3/4}$-dependent dissipative scales. To estimate λ_T, we write the kinetic energy dissipation rate as $\epsilon = 15\,\nu u^2/\lambda_T^2$ (Tennekes & Lumley 1972), assuming local isotropy, where u is the r.m.s. fluctuation of each component of velocity. We can cast this in terms of the centreline mean velocity, U_c, using the approximation $u/U_c \approx 0.2$ from the measurements of Everitt & Robins (1978) in a planar turbulent jet. This gives $\epsilon = 0.6\,\nu\,U_c^2/\lambda_T$, while in § 2.3.1, we wrote the dissipation rate in terms of outer-scale variables as $\epsilon \approx 0.019\,(U_c^3/\delta)$. Combining these expressions for ϵ gives

$$\frac{\lambda_T}{\delta} = 5.6\,Re_\delta^{-1/2}. \tag{4.2}$$

Comparing this with the expression for the Kolmogorov scale, η, in (2.7), we find

$$\frac{\lambda_T}{\eta} = 2.1\,Re_\delta^{1/4}, \tag{4.3}$$

and for Re_δ between 3290 and 8330 for the present data, this means that λ_T/η is between roughly 16 and 20. When the appropriate scaling coefficients are applied to relate η to the true dissipative scales λ_D and λ_ν, and to relate λ_T to a presumed true 'Taylor' scale, we cannot rule out the possibility that the resulting true Taylor scale might be smaller than the $Re_\delta^{-3/4}$-dependent dissipative scales. Even admitting this possibility, however, there is no indication in the data that $Re_\delta^{-1/2}$ scaling is significant in the scalar energy dissipation process. This can be seen in figure 12, where the thinnest dissipation layers also follow $Re_\delta^{-3/4}$ scaling.

4.1. *Universality of the scaling coefficient*

Besides confirming the $Re_\delta^{-3/4}$ scaling of the dissipation layer thickness, λ_D, the present measurements also provide an estimate of the proper scaling coefficient, Λ, in the thickness expression (1.8). The appropriate relation is

$$\lambda_D = 14.5\,\delta\,Re_\delta^{-3/4}Sc^{-1/2}, \tag{4.4}$$

where $\Lambda = 14.5$ is found from figure 11.

In the preparation of these experiments, the value $\Lambda = 11.2$ was used in estimating the resolution requirements for measuring the scalar gradient components $\partial C/\partial x_i$. This value of Λ was found through measurements of conserved scalar mixing in an axisymmetric co-flowing turbulent jet, at an outer-scale Reynolds number of 11 000 (Buch & Dahm 1998). In applying this Λ here, its value was interpreted as being general to different shear flows. For the present planar turbulent jet, we assumed that by defining the outer-scales similarly to Buch & Dahm in (1.8) (using the local jet centreline velocity as the velocity scale, U, and using the full width of the jet velocity profile at 5% of the centreline value as the flow width, δ), the value $\Lambda = 11.2$ gave the proper value of λ_D.

Recently, Tsurikov & Clemens (2002) measured a value $\Lambda = 7.8$ in the same axisymmetric co-flowing jet flow geometry used by Buch & Dahm (1998), at $Re_\delta = 8700$. The experiment of Tsurikov & Clemens was designed to achieve very high spatial resolution, so those authors concluded that the discrepancy between their measured value of Λ and that of Buch & Dahm is due to finite resolution effects in the earlier study. However, the value $\Lambda = 7.8$ measured by Tsurikov & Clemens is smaller than the value $\Lambda = 14.5$ measured here in a planar turbulent jet by a factor of 1.86. Before examining whether this difference can be solely explained by resolution effects, we consider another possibility, namely that the difference in Λ might partly be attributable to the different flow geometries considered.

In particular, the quantitative manner in which the outer-flow scales establish the turbulent fine scales appears not to be universally described using U and δ for different flows. The proper Λ to be applied in (1.8) thus seems to be flow-dependent. To illustrate this, we can consider how the Kolmogorov scale, η (or the Batchelor scale, η_B), relates to the outer-scale variables for different flows. The relation for planar jets was found in § 2.3.1 to be $\eta \approx 2.7\,\delta\, Re_\delta^{-3/4}$ for the present jet-to-ambient fluid density ratio of 1.54. Repeating the same analysis for axisymmetric jets, we begin with the following relation for the kinetic energy dissipation rate on the centrelines of axisymmetric turbulent jets, also measured by Antonia *et al.* (1980):

$$\epsilon \approx 48\,\frac{U_0^3}{d}\left(\frac{y}{d}\right)^{-4}, \tag{4.5}$$

with U_0 being the jet exit velocity, d the jet nozzle diameter and y the downstream coordinate. Using the relations $U_c = 6.2\,(\rho_0/\rho_\infty)^{1/2}\,U_0(y/d)^{-1}$ for the jet centreline velocity, and $\delta = \delta_{0.05} = 0.37\,y$ for the jet full width (Chen & Rodi 1980), and using $\rho_0/\rho_\infty = 1.54$ as for the present data, (4.5) gives $\epsilon \approx 0.039\,(U_c^3/\delta)$. Applied in (1.2), defining Re_δ as before in terms of U_c and δ, this gives

$$\eta \approx 2.3\,\delta\, Re_\delta^{-3/4}. \tag{4.6}$$

Equations (2.7) and (4.6) demonstrate that even when the outer-scale parameters of planar and axisymmetric jets are matched, the Kolmogorov and Batchelor scales will be larger in the planar jet by a factor of roughly 1.2. (Comparing (2.7) and (4.4), and using $Sc = 1.36$, the average dissipation layer thickness, λ_D, found from the present data is approximately 4.6 times the Kolmogorov scale, and 5.4 times the Batchelor scale.)

This result shows that it is impossible for the dissipation length scales, λ_v and λ_D, to be universally related to both the outer-scale parameters and the Kolmogorov/Batchelor scales. That is, the constants Λ and Λ_K appearing in (1.7) and (1.8) cannot both be universal and flow-independent. Because the Kolmogorov/Batchelor scales η and η_B are defined strictly in terms of quantities that are relevant at the small scales, and thus are independent of the details of the outer-flow scaling, we expect that Λ_K, which relates λ_v and λ_D to η and η_B, is universal. If this is true, then by (2.7) and (4.6), the appropriate Λ in (1.8) will be higher in planar jets by a factor of 1.2. This partially accounts for the discrepancy between the $\Lambda = 14.5$ found in these planar jet measurements and the $\Lambda = 7.8$ found in axisymmetric jets by Tsurikov & Clemens (2002), reducing the original factor of 1.86 discrepancy to a factor of 1.55. (Interestingly, this factor of 1.2 almost entirely accounts for the discrepancy between the $\Lambda = 14.5$ found here and the $\Lambda = 11.2$ found by Buch & Dahm 1998.)

In § 2.3.1 the in-plane grid spacing of the present data was found to be $\langle \Delta x/\eta \rangle = 1.07$. In comparison, Tsurikov & Clemens (2002) quote a grid spacing $\Delta x/\eta \approx 1.0$. Antonia & Mi (1993) investigated explicitly the effect of varied probe spacing on measurements of temperature dissipation rates, and found that differences of a factor of 2 in spacing accounted for perhaps a factor of 1.5 difference in the measured dissipation rates. Since the measured dissipation layer thickness can be expected to have a weaker dependence on grid spacing than the dissipation rate values themselves, it is unlikely that the difference in resolution accounts fully for the difference between the Λ value found here and that found by Tsurikov & Clemens (2002), even after the difference in flow geometry is taken into account.

Tsurikov (2002) has also presented scalar mixing results from an axisymmetric, co-flowing jet at $Re_\delta = 19\,000$, measuring $\Lambda = 10.6$. To explain the discrepancy between this Λ and the value of 7.8 measured by Tsurikov & Clemens (2002) at $Re_\delta = 8700$, Tsurikov (2002) hypothesized that the value of Λ itself may not be universal over all Reynolds numbers. In particular, the dissipation length scale λ_D may be given by (1.8), but with different values of Λ for different Reynolds number ranges. Higher values of Λ might be consistent with the greater scalar field homogeneity expected for Reynolds numbers beyond the mixing transition, for example. If true, the proper comparison for the value $\Lambda = 11.2$ of Buch & Dahm (1998) at $Re_\delta = 11\,000$ could be with the value $\Lambda = 10.6$ of Tsurikov (2002). While the present measurements show that λ_D is described well by (1.8) with a single value of Λ for Re_δ from 3290 to 8330, considerably higher Reynolds numbers would need to be considered to establish the Reynolds number (non-)universality of Λ.

5. Assessment of subgrid models

As pointed out in § 2.3, the scale separation between the large eddies and the scalar dissipation structures in a gas-phase turbulent flow is much smaller than the separation that would pertain in a liquid-phase flow at the same Reynolds number, owing to the much lower Schmidt numbers of gases. Gas-phase scalar imaging measurements can, therefore, more easily cover a range of length scales from the dissipation scale up to the integral scale. In the present measurements, the in-plane grid spacing of the data volumes is less than $0.5\lambda_D$, while the imaging planes span $> 0.67\delta$. This range of scales makes the data suitable for direct assessment of LES subgrid models for scalar mixing.

Approaches to LES of non-premixed combustion begin by computation of the mixture fraction. This is represented as a conserved scalar $C(\boldsymbol{x}, t)$, while the filtered mixture fraction computed directly by LES is written $\overline{C}(\boldsymbol{x}, t)$, where $C = \overline{C} + C'$. In general, the LES filtering operation is a density-weighted Favre filtering; however, because the present data are from a non-reacting incompressible flow, the $\overline{(\,)}$ operation will be treated as a simple grid filtering with characteristic filter width $\overline{\Delta}$. Non-premixed combustion models for LES then typically require knowledge of the subgrid scalar PDF. In the assumed-shape approach, the low-order statistical moments define the subgrid scalar PDF. Receiving much attention (Cook & Riley 1994; Jiménez *et al.* 1997) is the beta distribution, which is specified in each filter volume by the filtered scalar value, $\overline{C}$, which is known from the LES, and the filtered scalar variance, $\overline{C'^2}$, which can be written

$$\overline{C'^2} = \overline{C^2} - \overline{C}^2. \tag{5.1}$$

The first term on the right-hand side of this equation is not resolved by the LES, so $\overline{C'^2}$ must be modelled.

Here we consider two such models for the subgrid scalar variance. The first is the scale-similarity model of Cook & Riley (1994). Begin by defining $\widehat{(\,)}$ as an additional 'test' filter, with width $\widehat{\Delta}$, applied to the grid-filtered LES output. The scale-similarity model then assumes that $\overline{C'^2}$, the grid-filtered variance of C, is proportional to the test-filtered variance of $\overline{C}$. This can then be written in terms of LES-resolved quantities, as

$$\overline{C'^2} = \alpha_S(\widehat{\overline{C}^2} - \widehat{\overline{C}}^2), \tag{5.2}$$

where the proportionality constant α_S must be prescribed in the simulation. The second model is the gradient-based eddy-viscosity-type formulation described by Pierce & Moin (1998), where the subgrid variance is expressed as

$$\overline{C'^2} = \alpha_G \overline{\Delta}^2 |\nabla \overline{C}|^2 \tag{5.3}$$

with the constant α_G typically being found through the dynamic procedure.

5.1. A priori *testing*

Subgrid scalar variance models such as these can be tested by using spatially resolved scalar field data, where the $\overline{C'^2}$ field can be computed directly. The data are first filtered to mimic LES data, then (5.2) or (5.3) is applied, with the resulting model estimate of $\overline{C'^2}$ being compared with the exact values. Previous work has generally used direct numerical simulation (DNS) results for such *a priori* testing (e.g. Jiménez *et al.* 1997; Wall, Boersma & Moin 2000). Experimental scalar field data from liquid-phase flows have also been used (Cook & Riley 1994, data from Southerland & Dahm 1994), but the length scales covered by those data did not accurately reflect LES conditions (§ 2.3).

The models represented by (5.2) and (5.3) can be assessed through the correlation between the exact and modelled $\overline{C'^2}$, or through a comparison of the magnitudes. Magnitude agreement has a bearing on the values of the proportionality constants α_S and α_G. Specification of those constants is primarily a computational matter and will not be addressed in this paper. Instead we will focus on the structural accuracy of the models, as manifested through correlations.

The first step in the *a priori* testing is grid filtering the present experimental data to simulate LES results. Because the present data span only two planes in the out-of-plane direction, this grid filtering is limited to two-dimensional kernels. Here we use only square top-hat kernels. To be consistent with LES, the grid spacing of the grid-filtered data is the same as the kernel size. That is, while the experimental scalar field data, $C(\boldsymbol{x})$, are defined on a 220×220 grid, the grid-filtered data, $\overline{C}(\boldsymbol{x})$, are defined on a $(220/N) \times (220/N)$ grid, where N is the side length (in pixels) of the top-hat kernel. This ensures that $\overline{\overline{C}} = \overline{C}$, so (5.1) holds.

To test the scale-similarity model of (5.2), we will need to apply a test filter to both the grid-filtered data $\overline{C}$ and $\overline{C}^2$. Unlike the grid filtering, the test filtering is performed 'in place,' so the test-filtered data $\widehat{\overline{C}}$ and $\widehat{\overline{C}^2}$ are defined on the same grid as $\overline{C}$. This would not be done in an actual LES, but here increases the number of points available for computing statistics. The test filtering here also uses square top-hat kernels, and is implemented using Simpson's rule.

To assess the two models we will use the correlation, R^2, between the actual subgrid variance and the variance determined by each model:

$$R^2 = \frac{\left\langle \left(\overline{C'^2_A} - \left\langle \overline{C'^2_A} \right\rangle \right) \left(\overline{C'^2_M} - \left\langle \overline{C'^2_M} \right\rangle \right) \right\rangle^2}{\left\langle \left(\overline{C'^2_A} - \left\langle \overline{C'^2_A} \right\rangle \right)^2 \right\rangle \left\langle \left(\overline{C'^2_M} - \left\langle \overline{C'^2_M} \right\rangle \right)^2 \right\rangle}, \tag{5.4}$$

where $\overline{C'^2_A}$ is the actual subgrid variance at a given point in the grid-filtered domain, $\overline{C'^2_M}$ is the model estimate of the subgrid variance, and the brackets $\langle \cdot \rangle$ denote averaging over the full set of data. For the *a priori* testing, the grid filters used had sizes $\overline{\Delta} = 2$, 4, 8, 12, and 16 pixels on the original data grids. In terms of the estimated Kolmogorov

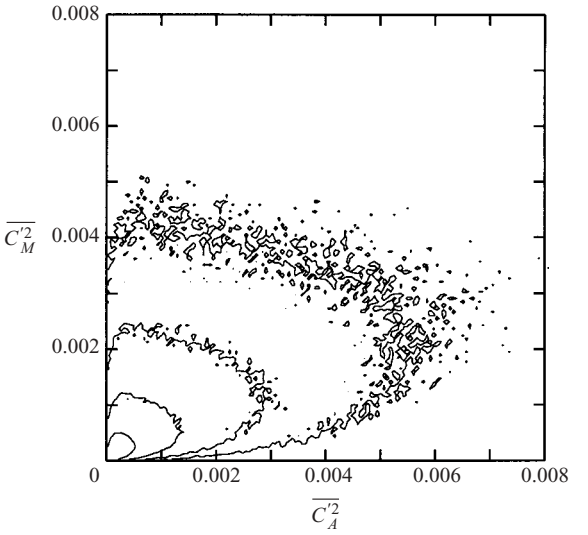

FIGURE 13. The joint PDF of the actual subgrid scalar variance, $\overline{C'^2_A}$, and the scalar variance estimated by the scale-similarity model, $\overline{C'^2_M}$, with grid filter size $\overline{\Delta} = 8$, and with a test filter spanning two pixels on the grid-filtered data grid. The contour scale is logarithmic, with adjacent contours representing a magnitude ratio of 5.

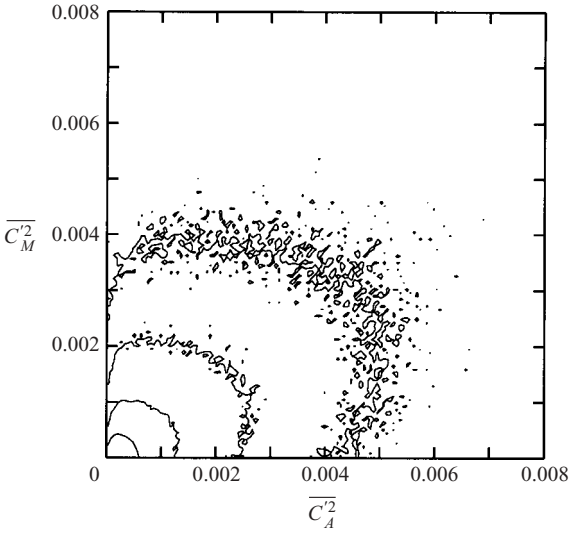

FIGURE 14. The joint PDF of the actual subgrid scalar variance, $\overline{C'^2_A}$, and the scalar variance estimated by the gradient-based model, $\overline{C'^2_M}$, with grid filter size $\overline{\Delta} = 8$. The contour scale is logarithmic, with adjacent contours representing a magnitude ratio of 5.

scale η (equation (2.7)), $\overline{\Delta}$ ranged from 3η to 23.7η. Figure 13 presents a contour plot of the joint PDF of $\overline{C'^2_A}$ and $\overline{C'^2_M}$ for the scale-similarity model, where the grid filter size is $\overline{\Delta} = 8$ and the test filter spans two pixels on the grid-filtered data grid. Figure 14 shows the joint PDF of $\overline{C'^2_A}$ and $\overline{C'^2_M}$ for the gradient-based model, again with grid filter size $\overline{\Delta} = 8$. In comparing these joint distributions, it appears that there is little to choose between the two models. If either model were to yield a perfect correlation

$\overline{\Delta}$ (pixels)	$\langle\overline{\Delta}\eta\rangle$	R_S^2	R_G^2	α_S	α_G
2	2.1	0.80	0.84	0.22	0.077
4	4.3	0.62	0.68	0.33	0.12
8	8.6	0.42	0.43	0.48	0.18
12	12.8	0.36	0.34	0.63	0.21
16	17.1	0.34	0.28	0.73	0.22

TABLE 3. Statistical results from *a priori* testing of the scale-similarity and gradient-based models for subgrid scalar variance (equations (5.2) and (5.3), respectively). The $\overline{\Delta}$ are the grid filter sizes used. $\langle\Delta/\eta\rangle$ is the average grid filter size normalized by the local value of the Kolmogorov scale, η. R_S^2 is the correlation between the true grid filtered variance, $\overline{C'^2}$, and the value estimated by the scale-similarity model. For the scale-similarity model, the test filter in all cases has a width of two pixels in the grid-filtered domain. R_S^2 is the correlation between the true $\overline{C'^2}$ and the estimate from the gradient-based model. Also given are the appropriate values of the proportionality constants α_S and α_G in (5.2) and (5.3) for each grid filter size.

between the modelled and measured $\overline{C'^2}$, then all contours would be confined to a straight line running through the origin. Neither model approaches this. While the contours of the joint PDF for the scale-similarity model appear to cover more of the $\overline{C_A'^2}$ vs. $\overline{C_M'^2}$ space, which would suggest a lower correlation between the actual and modelled variance, the gradient-based model notably overestimates the proportion of variance values near zero.

Table 3 gives the quantitative results for the *a priori* testing. For the scale-similarity model, the smallest possible top-hat test filter, spanning two pixels on the grid-filtered data grid, was found to give the best results, so only the results using that test filter are shown in the table. For the scale-similarity model, R_S^2 has a value of 0.80 for $\overline{\Delta} = 2$, dropping to $R_S^2 = 0.42$ for $\overline{\Delta} = 8$ and $R_S^2 = 0.34$ for $\overline{\Delta} = 16$. For the gradient-based model, $R_G^2 = 0.84$ for $\overline{\Delta} = 2$, $R_G^2 = 0.43$ for $\overline{\Delta} = 8$, and $R_G^2 = 0.28$ for $\overline{\Delta} = 16$. In terms of this correlation, (5.4), the two models perform similarly, although the gradient-based model is slightly superior for smaller grid filter sizes, while the scale-similarity model is slightly superior for larger $\overline{\Delta}$. These results suggest that the scale-similarity model should be preferred for those simulations that take advantage of the LES formulation by imposing a wide scale separation between the fine scales and the grid filter scale.

6. Conclusions

Measurements of the three-component scalar gradient field, ∇C, and scalar energy dissipation rate field, $\chi \equiv D\nabla C \cdot \nabla C$, permit investigation of the structural properties of fine-scale scalar mixing in gas-phase turbulent flows. The flow considered is a planar turbulent jet, with outer-scale Reynolds number ranging from 3290 to 8330. Despite the moderate Reynolds numbers, scalar power spectra for the data show some evidence of an inertial range of wavenumbers. The data confirm the tendency of the scalar dissipation rate fields to be organized into lamellar structures. Direct measurement of the average thicknesses of the dissipation layers, λ_D, indicates that $\lambda_D = 14.5\,\delta\,Re_\delta^{-3/4}Sc^{-1/2}$. The dependence on Re_δ (and δ) is consistent with the hypotheses of Kolmogorov and Batchelor. No evidence is found from the data that Taylor scaling ($\lambda_D \propto \delta\,Re_\delta^{-1/2}$) plays a significant role in the scalar dissipation process.

The scaling coefficient in the λ_D relation, $\Lambda = 14.5$, is slightly higher than the values found previously in round jets (Buch & Dahm 1998; Tsurikov & Clemens

2002; Tsurikov 2002). Careful reading of the results suggests that this coefficient, Λ, may not be universal for different flow geometries. It is more likely that a geometry-independent relationship exists between λ_D and the Kolmogorov and Batchelor scales, η and η_B. The present data show that $\lambda_D \approx 5.4\,\eta\,Sc^{-1/2} = 5.4\,\eta_B$, i.e. that the average layer thickness is roughly 5.4 times the Batchelor scale. While the present data confirm the $Re_\delta^{-3/4}$ dependence of λ_D with a single scaling coefficient, Λ, for Re_δ from 3290 to 8330, the recent results of Tsurikov (2002) at very high Reynolds number suggest that different values of Λ may be relevant in different Reynolds number regimes, perhaps separated by the mixing transition (Dimotakis 2000). Data for λ_D as a function of Re_δ for a wider range of Reynolds numbers than are available from the present data would be needed to address this.

The range of length scales resolved by the present data, from the dissipation scales up to nearly the full flow width, is well suited for *a priori* testing of subgrid models for scalar mixing in LES. Comparison of two models for subgrid scalar variance, a scale-similarity model and a gradient-based model, shows that the scale-similarity model is more accurate as the LES filter size increases. The scale-similarity model is thus preferred when the LES formulation is exploited by imposing a large separation between the fine mixing scales and the LES grid filter scale. *A priori* testing of this form can be very useful both in assessment and development of subgrid models for scalar mixing, which are necessary in combustion applications. For maximum flexibility, simultaneous scalar and velocity field measurements would be ideal, as this would allow investigation of quantities such as the subgrid scalar flux terms.

Financial support for this work was provided by the National Science Foundation (USA) through Grant No. CTS-9553124. The authors thank the reviewers for insightful comments.

REFERENCES

Antonia, R. A. & Mi, J. 1993 Temperature dissipation in a turbulent round jet. *J. Fluid Mech.* **250**, 531–551.

Antonia, R. A., Satyaprakash, B. R. & Hussain, A. K. M. F. 1980 Measurements of dissipation rate and some other characteristics of turbulent plane and circular jets. *Phys. Fluids* **23**, 695–700.

Bartels, J. *et al.*, (Eds.) 1962 *Landolt-Börnstein Numerical Data and Functional Relationships in Science and Technology* (ed. J. Bartels, H. Borchers, H. Hausen *et al.*), 6th Edn. Springer.

Batchelor, G. K. 1952 The effect of homogeneous turbulence on material lines and surfaces. *Proc. R. Soc. Lond.* A **213**, 349–366.

Batchelor, G. K. 1959 Small-scale variation of convected quantities like temperature in turbulent fluid. Part 1. General discussion and the case of small conductivity. *J. Fluid Mech.* **5**, 113–133.

Batchelor, G. K., Howells, I. D. & Townsend, A. A. 1959 Small-scale variation of convected quantities like temperature in turbulent fluid. Part 2. The case of large conductivity. *J. Fluid Mech.* **5**, 134–139.

Bradbury, L. J. S. 1965 The structure of a self-preserving turbulent plane jet. *J. Fluid Mech.* **23**, 31–64.

Buch, K. A. & Dahm, W. J. A. 1996 Experimental study of the fine-scale structure of conserved scalar mixing in turbulent shear flows. Part 1. $Sc \gg 1$. *J. Fluid Mech.* **317**, 51–71.

Buch, K. A. & Dahm, W. J. A. 1998 Experimental study of the fine-scale structure of conserved scalar mixing in turbulent shear flows. Part 2. $Sc \approx 1$. *J. Fluid Mech.* **364**, 1–29.

Bushe, W. K. & Steiner, H. 1999 Conditional moment closure for large eddy simulation of nonpremixed turbulent reacting flows. *Phys. Fluids* **11**, 1896–1906.

Catrakis, H. J. & Dimotakis, P. E. 1996 Mixing in turbulent jets: scalar measures and isosurface geometry. *J. Fluid Mech.* **317**, 369–406.

Chen, C. J. & Rodi, W. 1980 *Vertical Turbulent Buoyant Jets: A Review of Experimental Data*. Pergamon.

Clay, J. P. 1973 Turbulent mixing of temperature in water, air, and mercury. PhD thesis, University of California, San Diego.

Cook, A. W. & Riley, J. J. 1994 A subgrid model for equilibrium chemistry in turbulent flows. *Phys. Fluids* **6**, 2868–2870.

Corrsin, S. 1951 On the spectrum of isotropic temperature fluctuations in an isotropic turbulence. *J. Appl. Phys.* **22**, 469–473.

Dahm, W. J. A. & Buch, K. A. 1989 Log–normality of the scalar dissipation pdf in turbulent flows. *Phys. Fluids* A **1**, 1290–1293.

Dahm, W. J. A., Southerland, K. B. & Buch, K. A. 1990 Direct, high-resolution, four-dimensional measurements of the fine scale structure of $Sc \gg 1$ molecular mixing in turbulent flows. *Phys. Fluids* A **3**, 1115–1127.

Dimotakis, P. E. 2000 The mixing transition in turbulent flows. *J. Fluid Mech.* **409**, 69–98.

Dowling, D. R. 1991 The estimated scalar dissipation rate in gas-phase turbulent jets. *Phys. Fluids* A **3**, 2229–2246.

Dowling, D. R. & Dimotakis, P. E. 1990 Similarity of the concentration field of gas-phase turbulent jets. *J. Fluid Mech* **218**, 109–141.

Eckbreth, A. 1988 *Laser Diagnostics for Combustion Temperature and Species*. Kent, UK: Abacus Press.

Everitt, K. W. & Robins, A. G. 1978 The development and structure of turbulent plane jets. *J. Fluid Mech.* **88**, 563–583.

Gibson, C. H. 1968 Fine structure of scalar fields mixed by turbulence. II. Spectral theory. *Phys. Fluids* **11**, 2316–2327.

Gibson, C. H. & Schwartz, W. H. 1963 The universal equilibrium spectra of turbulent velocity and scalar fields. *J. Fluid Mech.* **16**, 365–384.

Gurvich, A. S. & Yaglom, A. M. 1967 Breakdown of eddies and probability distributions for small-scale turbulence. *Phys. Fluids* **10**, Suppl. Pt. II, S59–S65.

Jiménez, J., Liñan, A., Rogers, M. M. & Higuera, F. J. 1997 *A priori* testing of subgrid models for chemically reacting non-premixed turbulent shear flows. *J. Fluid Mech.* **349**, 149–171.

Kolmogorov, A. N. 1941*a* Dissipation of energy in the locally isotropic turbulence. *Dokl. Akad. Nauk SSSR* **32**, 16–18, English translation in *Proc. R. Sci. Lond.* A (1991) **434**, 15–17.

Kolmogorov, A. N. 1941*b* The local structure of turbulence in incompressible viscous fluid for very large Reynolds numbers. *Dokl. Akad. Nauk SSSR* **30**, 301–305, English translation in *Proc. R. Sci. Lond.* A (1991) **434**, 9–13.

Kolmogorov, A. N. 1962 A refinement of previous hypotheses concerning the local structure of turbulence in viscous incompressible fluid at high Reynolds number. *J. Fluid Mech.* **13**, 82–85.

Konrad, J. H. 1976 An experimental investigation of mixing in two-dimensional turbulent shear flows with applications to diffusion-limited chemical reactions. PhD thesis, California Institute of Technology.

Kotsovinos, N. E. & List, E. J. 1977 Plane turbulent buoyant jets. Part 1. Integral properties. *J. Fluid Mech.* **81**, 25–44.

Obukhov, A. M. 1949 Structure of the temperature field in turbulent flow. *Izv. Akad. Nauk SSSR Geogr. 1 Geofiz.* **13**, 58–69.

Obukhov, A. M. 1962 Some specific features of atmospheric turbulence. *J. Fluid Mech.* **13**, 77–81.

Peters, N. 1983 Local quenching due to flame stretch and non-premixed turbulent combustion. *Combust. Sci. Tech.* **30**, 1–17.

Pierce, C. D. & Moin, P. 1998 A dynamic model for subgrid-scale variance and dissipation rate of a conserved scalar. *Phys. Fluids* **10**, 3041–3044.

Prasad, R. R. & Sreenivasan, K. R. 1990 Quantitative three-dimensional imaging and the structure of passive scalar fields in fully turbulent flows. *J. Fluid Mech.* **216**, 1–34.

Reid, R. C., Prausnitz, J. M. & Poling, B. E. 1987 *The Properties of Gases and Liquids*, 4th Edn. McGraw-Hill.

Roshko, A. 1991 The mixing transition in free shear flows. In *The Global Geometry of Turbulence* (ed. J. Jiménez), pp. 3–11. Plenum.

Southerland, K. B. & Dahm, W. J. A. 1994 A four-dimensional experimental study of conserved scalar mixing in turbulent flows. *Tech. Rep.* 026779-12. University of Michigan.

Su, L. K. & Clemens, N. T. 1999 Planar measurements of the full three-dimensional scalar dissipation rate in gas-phase turbulent flows. *Exps. Fluids* **27**, 507–521.

Taylor, G. I. 1935 Statistical theory of turbulence. *Proc. R. Soc. Lond.* A **151**, 421–444.

Tennekes, H. & Lumley, J. L. 1972 *A First Course in Turbulence*. MIT Press.

Tsurikov, M. S. 2002 Experimental investigation of the fine-scale structure in turbulent gas-phase jet flows. PhD thesis, The University of Texas at Austin.

Tsurikov, M. S. & Clemens, N. T. 2002 The structure of dissipative scales in axisymmetric turbulent gas-phase jets. *AIAA Paper* 2002-0164.

Wall, C., Boersma, B. J. & Moin, P. 2000 An evaluation of the assumed beta probability density function subgrid-scale model for large eddy simulation of nonpremixed, turbulent combustion with heat release. *Phys. Fluids* **12**, 2522–2529.

Yip, B., Lam, J. K., Winter, M. & Long, M. B. 1987 Time resolved three-dimensional concentration measurements in a gas jet. *Science* **235**, 1209–1211.

Yip, B. & Long, M. B. 1986 Instantaneous planar measurement of the complete three-dimensional scalar gradient in a turbulent jet. *Opt. Lett.* **11**, 64–66.

Yip, B., Schmitt, R. L. & Long, M. B. 1988 Instantaneous three-dimensional concentration measurements in turbulent jets and flames. *Opt. Lett.* **13**, 96–98.